Solar Energy 287 (2025) 113203

Contents lists available at ScienceDirect

Solar Energy

journal homepage: www.elsevier.com/locate/solener

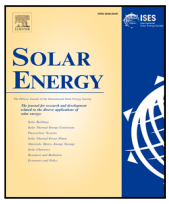

Neural-network-driven dynamic simulation of parabolic trough solar fields for improved CSP plant operation

Matthew J. Tuman, Michael J. Wagner *

University of Wisconsin-Madison, Department of Mechanical Engineering, 1500 Engineering Drive, Madison, 53706, WI, USA

ARTICLE INFO

Keywords:
Concentrating solar power
Dynamic simulation
Machine learning
Operations and maintenance
Training simulator
Parabolic trough

ABSTRACT

Concentrating Solar Power plants face challenges in achieving and sustaining high performance levels partially due to complexities in plant operations. This study addresses these challenges by developing a computationally efficient, high-fidelity parabolic trough solar field model capable of emulating CSP plant dynamics for use as an operator training simulator and as a tool for optimizing operation strategies. Leveraging a neural network methodology, the model efficiently computes heat absorbed by heat transfer fluid in a solar field with various receiver conditions. The trained neural network model achieves heat absorption error of 0.3% compared to a detailed model while increasing the simulation speed by a factor of 100. The solar field model is validated with data from the operational Solana Solar Generating Station near Gila Bend, AZ (US), and computes temperatures resulting in a mean absolute error of 2.2 [°C] over an entire day including start up and shut down. The model is further validated with respect to net optical efficiency that accounts for time-varying collector defocusing. Lastly, this work concludes with case studies that demonstrate the model's capabilities both as the engine for a training simulator and as an tool for optimizing solar field control strategies.

1. Introduction

Concentrating solar power (CSP) plants are of continued interest among renewable technologies because of their ability to incorporate thermal energy storage to improve dispatch capability and extend operation during periods of low insolation. However, achieving and maintaining a high level of performance in large-scale and complex CSP plants is challenging. The substandard performance of some existing CSP plants in the U.S. partly stems from the ongoing maturation of technology which will naturally improve over time with more operational experience. However, performance improvement can also be tied to a need for more complete and timely operator skill development [1]. Thus, this work aims to develop a parabolic trough solar field model that emulates CSP plant dynamics at sufficient temporal and spatial resolution for use in a detailed operator training simulator and for assessing operational strategies.

The parabolic trough solar field is comprised of numerous solar field loops in parallel that, together, collect the solar thermal energy for use in a Rankine cycle power block. Each loop contains multiple solar collector assemblies (SCA's) in series, each equipped with their own tracking drive and heat transfer fluid (HTF) temperature sensor. Cold HTF is distributed to the solar field via a supply header pipe. Once the HTF is heated in the loops, it returns back to the plant via a hot header pipe where, depending on the mode of operation, it can be used to generate superheated steam for the Rankine cycle, heat a secondary fluid for thermal energy storage, or be recirculated back to the solar field. While the thermal energy storage and the power block are key components of the plant, this work focuses on the development of a solar field model. Most parabolic trough collector (PTC) plant models include the solar field, but this work also includes more detailed models of often overlooked equipment such as control valves, main HTF pumps, piping at the central plant, and an HTF expansion management system.

PTC solar field modeling has evolved significantly from seminal models like NREL's *Excelergy* that was based on empirical curves from operational plants [2,3]. To overcome limitations in evaluating new technologies, the physical trough model in System Advisor Model (SAM) was developed [4] which incorporated first principles to capture detailed thermal behaviors of solar fields. The physical trough model, despite extrapolating field performance from the simulation of a few representative loops, remains a versatile tool as it employs the Forristall model to compute receiver heat loss under various conditions [5]. Concurrently, in Spain, a sophisticated model was created using Mathematica 7 and validated with plant data [6]. Unlike SAM, this model can simulate transient events with short time steps. Nonetheless, both models include hydraulic solvers for HTF flow

* Corresponding author.
E-mail address: mjwagner2@wisc.edu (M.J. Wagner).

https://doi.org/10.1016/j.solener.2024.113203
Received 13 August 2024; Received in revised form 13 November 2024; Accepted 13 December 2024
Available online 6 January 2025

Nomenclature

ANI	Aperture-normal irradiance
CSP	Concentrating solar power
DLR	German Aerospace Center
DNI	Direct normal irradiance
HCE	Heat Collection Element
HTF	Heat transfer fluid
NN	Neural network
NPSHR	Net-positive suction head-required
NREL	National Renewable Energy Laboratory
PTC	Parabolic trough collector
SCA	Solar collector assembly
VSF	Virtual Solar Field

rates that assume perfect operator control [4,6]. More recently, many researchers are using Dymola and Modelica. Specifically, numerous studies investigating parabolic trough systems utilized the open-source ThermoCycle library [7–11]. The parabolic trough collector model in the ThermoCycle library uses the Forristall model or empirical curve fits to compute heat absorbed by the HTF.

The most advanced high-fidelity transient simulation tool for CSP training is the Virtual Solar Field (VSF) developed by the German Aerospace Center (DLR). VSF integrates a hydraulic solver and a thermal model to compute HTF temperatures for all loops in a solar field [12–14]. Despite its effectiveness, several limitations with respect to the present work are noted: first, VSF's curve relating SCA defocusing to optical efficiencies is generic [12], while the present work uses SolTrace [15] to develop plant-specific defocusing curves, providing an accurate and adaptable method for other plants. Additionally, the current work is written in FORTRAN for TRNSYS integration and, similar to the ThermoCycle library, will be open sourced for other TRNSYS users. This facilitates easy adaptation with existing or new power block models in TRNSYS, unlike the C++ model used in VSF. Also, the present model includes HTF network components such as variable speed pumps and expansion systems which are crucial for maintaining optimal pressure and preventing issues such as pump cavitation.

Furthermore, the current work presents a novel approach using neural networks to efficiently compute heat loss in the solar field under various receiver conditions, whereas VSF uses empirical curves for pristine receivers. The ability to simulate heat collecting elements in a non-pristine state is particularly relevant for aging plants, and it produces a more realistic population of loop outlet temperatures.

There have been numerous applications of neural networks (NN) in CSP [16]. For example, a neural network was used to predict outlet temperatures in flat-plate solar collectors based on experimental data [17]. Additionally, data clustering has been used to improve CSP simulation efficiency [18,19]. The approach presented here differs from these prior works in that a NN is used to replace a computationally expensive energy balance solver.

Contribution to literature:. This work builds upon the current state of the art by utilizing a multi-variate NN methodology to predict heat loss for receivers in varying conditions. For example, this approach addresses the limitation of [13], which relies on a single-variable empirical fit to compute heat loss for pristine receivers. Additionally, compared to the Forristall model, the proposed methodology is 100 times faster while maintaining an average error of 0.3%. This speed improvement enables direct simulation of all loops in the solar field rather than modeling only a subset and extrapolating total field performance as done in [4]. Moreover, this advancement improves upon [7] by enabling fast and highly detailed simulations without relying on empirical curves that compromise accuracy or model flexibility.

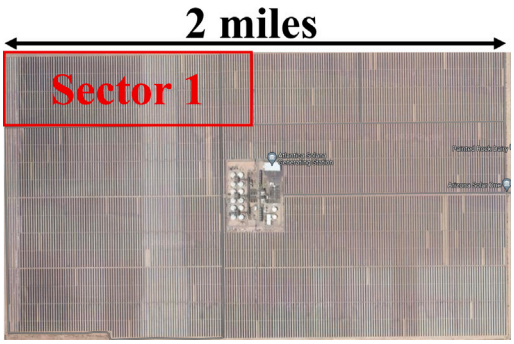

Fig. 1. Satellite image of Solana outlining one of eight sectors.

2. Methodology

The solar field model in this work was developed in TRNSYS which is a FORTRAN-based software tool designed for transient simulations [20]. TRNSYS users have the ability to define *Types* which are computational modules that receive inputs, perform calculations, and return one or more outputs. A TRNSYS system model is constructed by connecting outputs of *Types* to inputs of other Types. The methodologies discussed in the following sections are implemented with user-defined *Types*.

The solar field developed in the present work is modeled after Solana—a 280 MW parabolic trough plant in Gila Bend, AZ that utilizes thermal oil as the HTF. While the model is, in principle, flexible and can be configured to resemble a variety of plants, the results presented herein are compared against Solana data. A satellite image of Solana in Fig. 1 [21] illustrates the scale of the site and highlights a single sector, which is the largest repeating structure in the solar field.

Solana is the largest CSP plant in the U.S. and occupies a land area that is about 2 square miles. The solar field is arranged into eight sectors each using an inlet header pipe and return header pipe to connect up to 104 solar field loops in parallel. Each loop consists of four solar collector assemblies (SCA's) that have separate tracking drives that can be used to position the collector and defocus the SCA if the HTF is overheating.

2.1. Hydraulic solver

The HTF pumps, valves, headers, loops, bypass lines, and connections form a complex hydraulic network through which flow must be computed at each time step. This work utilizes an iterative method to solve for HTF flow rates while ensuring that: (i) mass flow entering a node equals the mass flow exiting (conservation of mass); (ii) the total pressure loss experienced by the fluid exactly equals that provided by the pump (conservation of energy); and (iii) the pressures of two fluids converging at a tee are equal.

The flow rate solution is affected by operator decisions such as pump speeds and valve positions as well as the thermal state of the HTF throughout the plant. Flow rates are computed using a form of the Linear Theory Method [22] which accommodates the complex system of non-linear equations involving pressure drop and mass flow. The Linear Theory Method linearizes a portion of the model in order to produce a system of linear equations which is then used to iteratively solve for the appropriate flow rate values. An example of the approximation is presented in Eq. (1) which constrains the pressure drop across two piping branches, ΔP_1 and ΔP_2, to be equal.

$$\Delta P_1 - \Delta P_2 = K_1 \dot{m}_1^2 - K_2 \dot{m}_2^2 \approx (K_{1,i-1} \dot{m}_{1,i-1}) \dot{m}_{1,i} - (K_{2,i-1} \dot{m}_{2,i-1}) \dot{m}_{2,i} = 0 \quad (1)$$

In this equation, $K_{x,y}$ is the pressure loss coefficient and $\dot{m}_{x,y}$ is the mass flow rate across piping branch x for iteration y. The values of

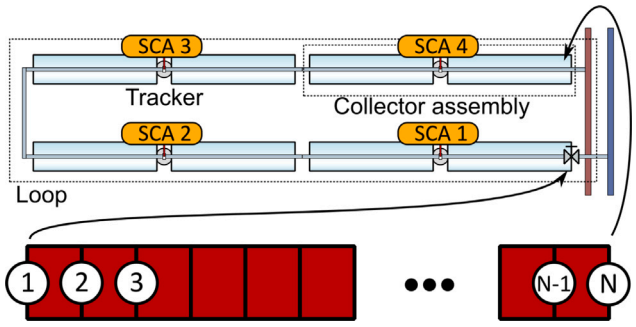

Fig. 2. Discretization of solar field loop into $N-1$ control volumes.

$K_{x,y}$ are a function of the mass flow through the piping branch, so an initial guess is provided for $\dot{m}_{1,0}$ and $\dot{m}_{2,0}$ which yields a solution for $K_{1,0}$ and $K_{2,0}$. With these variables estimated, subsequent iterations update the guessed mass flow rates, $\dot{m}_{1,1}$ and $\dot{m}_{2,1}$, and the process repeats until convergence. In this work, the methodology is used to solve for 19 mass flow rates while accounting for main HTF pump speeds, valve positions, and the pressure set by the expansion tanks. The solver typically achieves convergence within 10 iterations or less, and this iteration and convergence is repeated for each time step as conditions change.

This approach extends the work of similar hydraulic model implementations in existing literature [12] by accounting for the fluid level in the expansion tank to predict pump cavitation. Expansion systems are required in practice due to large temperature-dependent volume variation of the HTF between nighttime and daytime operations. For example, the density of Therminol-VP1 varies from $\rho = 1000$ [kg/m^3] at $T = 100$ [°C] to $\rho = 756$ [kg/m^3] at $T = 350$ [°C]. The volume of fluid in the active flow loop must be constant to avoid air gaps that could cause pump cavitation, fluid hammer, or loss of heat transfer during startup, so the total mass of fluid in the system significantly exceeds the amount needed during normal operation when the average temperature of HTF in the system is at its highest. While design of the expansion system varies to some degree, it is generally true that the expansion tanks dictate the HTF pressure at the inlet of the main HTF pumps where the expansion line is connected to the main flow network. This inlet pressure is highly relevant for predicting pump cavitation. The pump manufacturer's net-positive suction head required (NPSHR) curve specifies the required HTF inlet pressure as a function of flow rate. Therefore, given a pump speed and inlet pressure determined by the level of HTF in the expansion tank, the model predicts whether the pumps will cavitate based upon the NPSHR curve. This capability is valuable for capturing operational scenarios in which excessive pump speed in combination with inadequate level in the expansion tanks results in damage to the plant's main HTF pumps.

2.2. Solar field loop thermal model

While the hydraulic model is used to solve for flow rates through the various branches of the piping network, a thermal model is required to predict heat addition and to capture the energy state of the system. A finite volume approach is utilized to compute the temperatures of the HTF in a solar field loop. This is accomplished by first discretizing the solar field loop into a user defined number of control volumes as illustrated in Fig. 2. Also presented in Fig. 2 is a schematic of a solar field loop. The SCA's are labeled sequentially from the inlet to the outlet.

Nodal temperatures are computed at the interface of the control volumes instead of at the center. This subtle but important difference in approach has advantages for control volumes that have a linear temperature gradient between the inlet and outlet. By tracking the boundary temperatures instead of the mean control volume temperature, the simulation maintains good stability for coarser spatial discretizations, allowing for faster solve times. The energy balance for a loop control volume is expressed in Eq. (2).

$$\dot{m}\ h_i + \dot{q}_{in} = C_{pipe}\ Vol\ \rho\ \bar{c}\ \frac{\partial \bar{T}}{\partial t} + \dot{m}\ h_{i+1} \tag{2}$$

Here, $\dot{q}_{in}$ represents the thermal energy absorbed by the HTF, $\bar{c}$ is the specific heat of the HTF evaluated at the average temperature of nodes i and $i+1$, h_i is the enthalpy of the HTF evaluated at the temperature of the ith node, and $\frac{\partial \bar{T}}{\partial t}$ is the average temperature rate of change of the control volume.

The unitless parameter C_{pipe} represents the thermal capacitance of the piping in the solar field loops and is determined empirically with operational data. The choice of C_{pipe} has a significant effect on the dynamic response; a higher value results in a slower response of the HTF temperature to changes in solar heating, whereas a lower value leads to a quicker response. The control volume temperature rate of change can be algebraically rearranged from Eq. (2) to yield Eq. (3), assuming fluid incompressibility.

$$\frac{\partial \bar{T}}{\partial t} = \frac{1}{C_{pipe}\ (Vol)\ \rho\ \bar{c}}(\dot{m}\ \bar{c}\ (T_i - T_{i+1}) + \dot{q}_{in}) \tag{3}$$

The difference between inlet and outlet enthalpies is approximated with $\bar{c} \cdot \Delta T$. The placement of temperature nodes at the control volume boundaries means that the time rate of change of a tracked node is dependent on the mean temperature of both of the adjacent control volumes. Therefore, the nodal temperature rates of change are computed by averaging the control volume temperature rates to the left and right of the node of interest, as illustrated in Eq. (4). The temperatures of each node are stepped through time using the 4th-order Runge–Kutta method with the nodal temperature derivatives.

$$\frac{\partial T_i}{\partial t} = \frac{1}{2}\left[\left(\frac{\partial \bar{T}}{\partial t}\right)_{LHS} + \left(\frac{\partial \bar{T}}{\partial t}\right)_{RHS}\right] \tag{4}$$

2.3. Receiver heat loss model

The ability to capture realistic solar field behavior is dependent upon the accurate computation of the heat absorbed by the HTF, $\dot{q}_{in}$. This computation is typically performed using the Forristall model [5]. While the Forristall model has been validated and is considered accurate, it is computationally expensive when applied to many control volumes and precludes use in high-fidelity, real-time simulation. Thus, we employ a NN surrogate model to more efficiently compute the heat absorbed by the HTF ($\dot{q}_{in}$) as a function of HTF temperature (T_{HTF}), ambient conditions (T_{amb}, T_{sky}, v_{wind}), HTF mass flow ($\dot{m}_{HTF}$), gas pressure in the annulus (P_a), and solar energy incident upon the absorber ($\dot{q}_{solar}$). As such, the computation of $\dot{q}_{solar}$ accounts for optical efficiencies consistent with the method used in SAM [4]. A notional representation of the neural network utilized is illustrated in Fig. 3.

The architecture used in this work uses seven hidden layers with the number of nodes per layer ranging from six to two. Each hidden layer is fully connected. All 7 hidden layers utilize the *ReLU* activation function to facilitate non-linearity. However, the last layer, which computes the prediction for heat absorption, uses a linear activation function following common practice in NN regression applications. The specifics of the neural network architecture are presented in Table 1.

Table 1
Neural network architecture utilized to compute heat absorption.

Layer	1	2	3	4	5	6	7	8
Nodes	5	6	4	5	4	3	2	1
Act. Function	ReLU	ReLU	ReLU	ReLU	ReLU	ReLU	ReLU	Linear

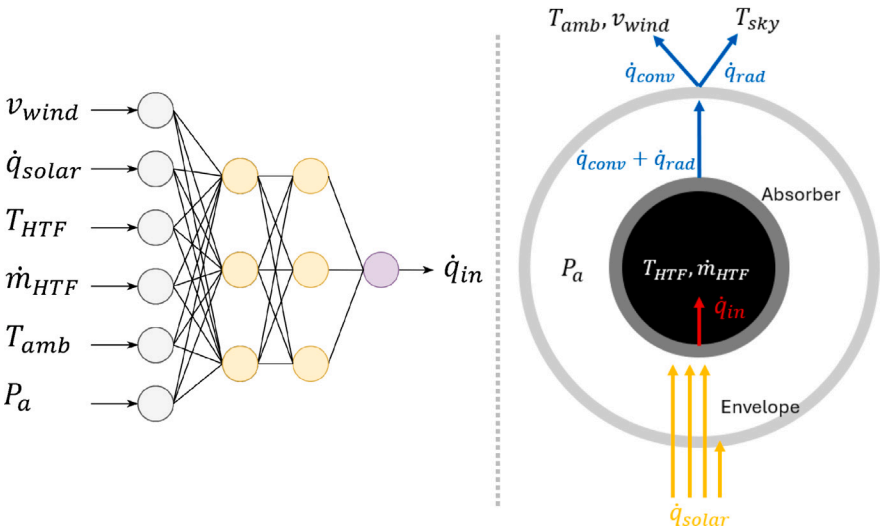

Fig. 3. Visual representation (not to scale) of neural network used to predict HTF heat absorption (left) and Forristall model energy balance (right).

Table 2
Range limits for the NN training dataset, and number of discretization points for each receiver condition.

	v_{wind} m/s	DNI W/m^2	T_{HTF} K	$\dot{m}_{HTF}$ kg/s	T_{amb} K	P_a torr
Range bounds						
Min.	0.5	0	470	0.5	273	0.001
Max.	13	1100	675	9	323	1
Discretization count by receiver condition						
Pristine	6	20	20	5	6	1
Broken glass	10	28	28	7	28	1
Hydrogen	8	21	21	5	12	8
Lost vacuum	6	20	20	5	6	1

Two points bear further consideration with respect to NN implementation. Firstly, a separate NN needs to be trained for each heat collection element (HCE) condition—four, in this case—due to the distinct performance characteristics associated with each (pristine, broken glass, lost vacuum, and hydrogen permeation). Secondly, a reliable and effective method for training the NN is of paramount importance in ensuring that heat absorption is accurately predicted across a wide range of simulation conditions. The NN training dataset covers input values within their specified ranges across a multi-dimensional grid. Each input variable is linearly discretized between its minimum and maximum values. For every combination of input values on this grid, the heat input $\dot{q}_{in}$ is computed using the Forristall model. The NN is thereby trained to replicate the output of the Forristall model. Table 2 lists the input variable ranges and the number of discretization points used to generate the grid space for the training data.

The bounds defined in Table 2 are derived from historical weather data along with inherent physical limitations. For example, there is a maximum amount of direct normal irradiance (DNI) that can be incident upon Earth's surface. Furthermore, the maximum wind speed for the training data is set to the stow limit which is a wind speed at which trough plants defocus collectors to protect them from aerodynamic-induced stresses.

Of equally importance are the number of training data values included within the bounds. Each dimension is linearly discretized according to the number of proscribed values, with the number used depending on the impact the variable has on the computation of $\dot{q}_{in}$. The importance of each variable can change with receiver condition, so more or less values are needed to resolve behaviors of interest. For example, heat loss is high in a receiver with hydrogen in the annulus space, and performance strongly depends on ambient conditions. Thus, the training dataset corresponding to the NN with hydrogen must have more ambient condition data points to accurately compute heat loss across a wide range of operating conditions in comparison to the pristine receiver. For reference, the pristine receiver neural network requires a dataset with 72,000 samples, and the hydrogen receiver neural network requires 1,700,000 samples.

Data pre-processing is required after training datasets have been generated to normalize and scale values of different dimensions. The min–max scaling method is chosen as it reflects the linearly distributed distribution of the input values. Scaling is applied to both the inputs and the outputs of the neural network. The normalization function used is provided in Eq. (5).

$$\hat{x} = \frac{x - x_{min}}{x_{max} - x_{min}} + 0.1 \tag{5}$$

This scaling method reduces all inputs and outputs used for training to the range between 0.1 and 1.1. The normalization offset of 0.1 is applied to accommodate the infrequent but possible case that input values fall below the minimum bound; specifically, this could be the case for ambient temperature and HTF temperature. Maintaining positive input and output values improves the fit result in scenarios that fall outside the bounds of the strictly defined training set.

The model presented in this work is accompanied by a set of scripts that automatically create and train the NN's for new receiver geometries, material properties, or states. The NN training process involves finding optimal weight values using gradient descent, which is implemented using the TensorFlow library in Python. The weights in the model are initialized using He Uniform scaling [23], and the weights are optimized using the adaptive moment estimation (Adam) [24] with a fixed learning rate of 0.001 and zero dropout. Each NN is trained over 12 epochs using mini-batches of 64, with the dataset split into 80% for training and 20% for validation. The performance of each NN is evaluated using the mean squared error (MSE), and the weight values that yield the lowest validation error are selected. Training was conducted on a system with an Intel i7-13620H processor and 16 GB of RAM. A summary of the training time and error metrics of the NN's used in this work is presented in Table 3.

The reported MSE values are based on a normalized range of 0.1 to 1.1. Although validation set errors are consistently higher than training set errors, both remain small compared to accuracy requirements for the model application of heat loss estimation. Given the scaled output data, these errors correspond to percent differences of less than 0.5%. To further ensure no overfitting occurs, we test the NN's with data

Table 3
Summary of neural network training for the different HCE states.

State	Number of training samples [–]	Training set error [–]	Validation set error [–]	Training time [min]
Pristine	72,000	6.9e−06	2.7e−05	0.26
Broken glass	1,536,640	7.9e−06	3.8e−05	9.07
Hydrogen	1,693,440	1.5e−05	2.8e−05	9.4
Lost vacuum	72,000	4.3e−06	1.3e−05	0.85

outside the training set and from a secondary source, which will be discussed in more detail in Section 3.1. Next, the reported training time includes both the time taken to generate the training datasets and the time required to train the NN's. In total, the entire data generation and training process requires approximately 20 min on the hardware previously described.

The primary motivation for developing the NN fit approach was to drastically reduce simulation runtime while maintaining a high degree of accuracy. The full Solana solar field was simulated first using the Forristall model and again using the NN approach. The Forristall model simulation required 5.25 s per time step, whereas the NN simulation approach required 0.05 s per time step. Thus, the neural network approach decreases the simulation runtime by two orders of magnitude. A method and source code for generating NN for additional scenarios is provided in [25].

Lastly, the flexibility of the NN model is limited to the dimensions varied within the training dataset, including weather input, HTF temperature and flow, and receiver state conditions. Other geometric and thermal property considerations are linked to the specific NN instance trained for the given case, and care must be taken to properly define the receiver properties in the physical model that provides data to the NN to ensure the model aligns with the application of interest. The primary objective of this NN model is not to serve as a generalized model for all real systems but rather to offer a significantly accelerated version of the established Forristall model, which has been widely used in both industry and research [4,7]. The overall receiver heat loss predicted by the Forristall model has been experimentally validated to within ±10 W/m or approximately 2.9% [26], though additional uncertainty is introduced *in situ* by way of unknown surface emissivities, fouling resistance, or annulus pressure, to name a few. The present work does not aim to further validate or improve the accuracy of the underlying physical model, but instead aims to reduce computational time for a high-volume model calculation while maintaining fit error below the validation uncertainty level. Future work may explore a more generalized NN model, but would require a shift towards training from measured data from multiple receiver types operating under a variety of conditions.

2.4. Solar field sector model

The solar field sector model simulates numerous solar field loops connected by inlet and return headers. The methodology used to compute pressure drops in a sector follows closely the approach used by the physical trough model in SAM [4]. There are two main components of the sector that require pressure drop computation. The first is pressure drop through the pipes due to frictional losses.

$$\Delta P_{pipe} = \frac{f\ \rho\ L_{pipe}\ v_{ave}^2}{2\ D_{pipe}} \tag{6}$$

This pressure drop computation is dependent upon the diameter of the pipe (D_{pipe}), average velocity of the fluid through the pipe (v_{ave}), pipe length (L_{pipe}), density of the fluid (ρ), and friction factor (f) which is computed using the Colebrook formulation.

The other pressure drop in the sector is due to form losses such as fittings, elbows, and valves. Each type of form loss is characterized using a loss coefficient, $k_{\Delta P}$. The values for these loss coefficients are identical to those used in the physical trough model [4]. The calculation used to compute pressure drops across these piping components is formulated in Eq. (7).

$$\Delta P_i = \frac{1}{2} k_{\Delta P,i}\ \rho\ v_{ave}^2\ N_i \tag{7}$$

This equation computes the pressure drop across the ith piping component. The only new variable here is N_i which represents the number of the ith component in the piping section of interest. Therefore, the model keeps track of how many of each piping components are within each piping segment.

Using Eqs. (6) and (7), the pressure drop is computed for each section of the sector. Specifically, each sector has a cold header (hdr,c), hot header (hdr,h), inlet/outlet/cross-over piping ($IOCop$), and solar field loop ($Loop$). With the pressure drop across each section determined, the total pressure drop across a solar field sector is computed with Eq. (8).

$$\Delta P_{sector} = \Delta P_{Loop} + \Delta P_{hdr,c} + \Delta P_{hdr,h} + \Delta P_{IOCop} \tag{8}$$

For the pressure drop computation, it assumed that HTF flow into a solar field sector is equally distributed across all the loops in the sector. This decision was driven by the fact that, at most large-scale CSP plants, operators do not have the ability to easily modulate individual solar field loop control valves over the course of a single day. Operators can instead adjust flow rates to the various sectors by using sector control valves.

Next, the thermal behavior of header pipes and all solar field loops (up to 104 loops per sector at Solana) are modeled independently to better capture real system behaviors. The only difference with the header thermal model is that heat loss is assumed to be a constant value in units of [W/m]. Also, the computational expense of simulating all solar field loops each with unique receiver states is significant, but the model solves faster than real-time owing largely to the computational efficiency introduced by the neural network approach. To make the thermal model even more realistic, inter-loop flow variability is subsequently introduced for each loop using Eq. (9).

$$\dot{m}_{i,t} = \frac{\dot{m}_{sector,t}}{n_{loops}}(1 + \mathcal{N}(0,\sigma^2)) \tag{9}$$

The flow rate for the ith loop at the tth time step, $\dot{m}_{i,t}$, is determined based on the average flow rate through a loop ($\dot{m}_{sector,t}/n_{loops}$) multiplied by a randomly-sampled adjustment factor. At the beginning of the simulation, this factor is generated for each loop from a zero-mean normal distribution with a standard deviation of σ. Because the distribution is normal, around 95% of the loops in the sector will have a mass flow rate within $\pm 2\sigma$ of the average.

The HTF temperatures at the outlet of each solar field loop must be controlled to avoid exceeding the temperature limit that leads to HTF degradation. Heat absorption in solar field loops is limited using defocusing, a strategy in which SCA collector drives are actuated to move the absorber element slightly or entirely out of the focal region of the parabolic mirror. The defocusing algorithm can vary by plant; the method implemented in the present work is outlined below.

- If $T_{outlet} > T_{limit}$, Then the last two SCA's will defocus 0.8° ($\eta_{SCA} = 0.4$)
- If $T_{outlet} > T_{limit} + 2.0$ [K], Then the last two SCA's will defocus 1.2° ($\eta_{SCA} = 0.1$)

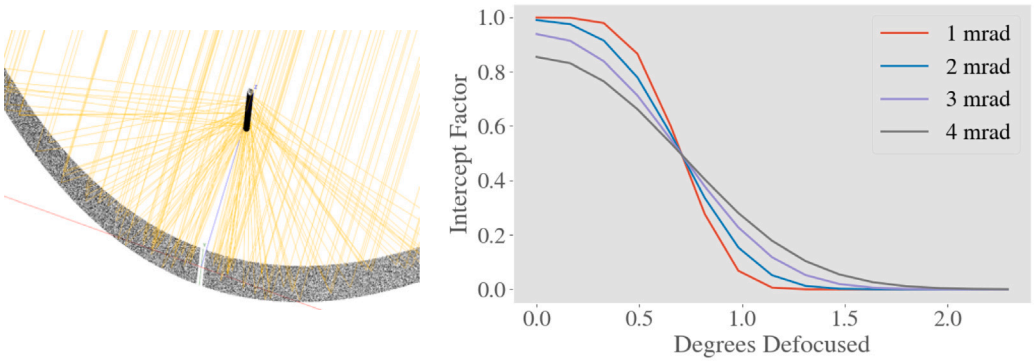

(a) Rendered ray paths and intersections in SolTrace

(b) Computed intercept factors as a function of degrees defocused and surface slope error magnitude.

Fig. 4. Characteristics of the collectors used at Solana.

- If $T_{outlet} > T_{limit} + 4.0$ [K], Then the last two SCA's will defocus 2.0° ($\eta_{SCA} = 0.0$)
- If $T_{outlet} > T_{limit} + 6.0$ [K], Then all SCA's will defocus 2.0° ($\eta_{SCA} = 0.0$)

Here, T_{outlet} is the loop outlet temperature, T_{limit} is the HTF temperature limit defined by the user, and η_{SCA} is the optical efficiency of the SCA given the current amount of defocusing. For example, if 1000 [W/m^2] is incident upon an SCA that is defocused 0.8°, then the energy incident upon the receiver is 400 [W/m^2]. The optical efficiency of the SCA, η_{SCA}, accounts for the proportion of reflected light that hits the receiver, a quantity referred to as an *intercept factor*. These intercept factors are unique to collector geometries and the number of degrees that the collector is defocused. The intercept factors were computed using SolTrace which is a Monte-Carlo ray tracing software specifically designed for CSP applications [15]. Fig. 4 presents an illustration of the Monte-Carlo ray tracing method utilized by SolTrace along with the computed intercept factors for the specific collector geometry used in this work. The various intercept curves correspond to different surface slope error values.

3. Validation

This section presents aspects of model validation which ensures good behavioral agreement between the simulation and observed trends and values from an operating facility. The goal of this validation is not exact agreement in model results, but rather, accurate representation of the plant response to changes in state or operating conditions; this is consistent with the goal of using the model as an operator training tool. We first validate the neural network model to ensure good agreement with the more detailed, physics-based Forristall model, then present validation of a solar field sector, which is the broadest repeatable unit found in the solar field.

3.1. Neural network validation

The data used in this validation study consists of historical weather measurements from Gila Bend, AZ. The validation data is separate from the training dataset, allowing for an assessment of potential overfitting via the following method. Solar field loops comprised of the four distinct receiver states were simulated using weather data from three separate days and one second time steps. For example, one loop is comprised of receivers that are all pristine, and another loop has receivers that all have 0.1 torr of hydrogen in the annulus space, etc. For each loop and day, the NN and the Forristall model each separately computed the heat absorption by the HTF, the latter serving as the basis for comparison. Eq. (10) quantifies the results in terms of a normalized root-mean-squared difference.

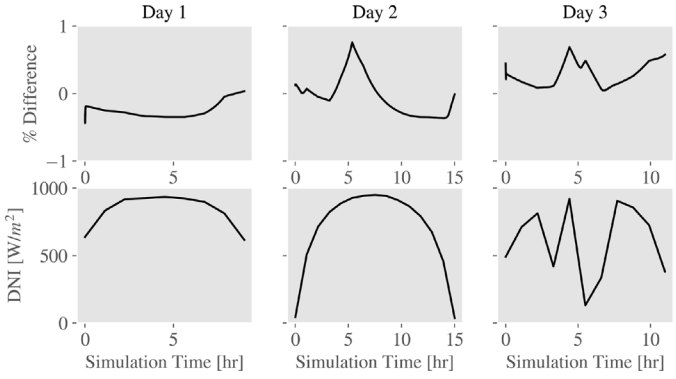

Fig. 5. Neural network validation study illustrating the difference in the computed heat absorbed by an entire loop using the Forristall model and the neural network.

$$error\ [\%] = \sqrt{\frac{1}{n_{time}} \sum_{i=1}^{n_{time}} \left(\frac{\dot{q}_{NN,tot,i} - \dot{q}_{F,tot,i}}{max(\dot{\mathbf{q}}_{F,tot})} \right)^2} \cdot 100\ [\%] \tag{10}$$

Here, $\dot{q}_{F,tot,i}$ is the total heat absorbed by the solar field loop at time step i computed using the Forristall model, $\dot{q}_{NN,tot,i}$ is the heat absorbed by the solar field loop at time step i predicted by the neural network, and n_{time} is the number of time steps in the simulation. This metric captures the average loop heat absorption error throughout the day as a percentage of the maximum heat absorbed during a single time step.

The largest observed error was 1.2% and the average difference for the 21 simulations performed was 0.3% indicating that the NN approach is accurate with reference to the Forristall model. Fig. 5 presents the difference between heat absorbed by a solar field loop using the neural network and the Forristall approach. Three days are presented along with the different solar conditions. For reference, in these simulations the loop is comprised of receivers with 0.1 torr of hydrogen in the annulus space.

In Fig. 5, the columns correspond to the day simulated. The top row presents the percent difference between heat absorbed using the Forristall model and the NN using Eq. (10). Day 3, representative of a cloudy day, illustrates the NN's capability to provide performance predictions consistent with the Forristall model over a wide range of operating conditions. All three of these simulations have differences near 0.3%, thereby accurately predicting heat absorption relative to the Forristall model.

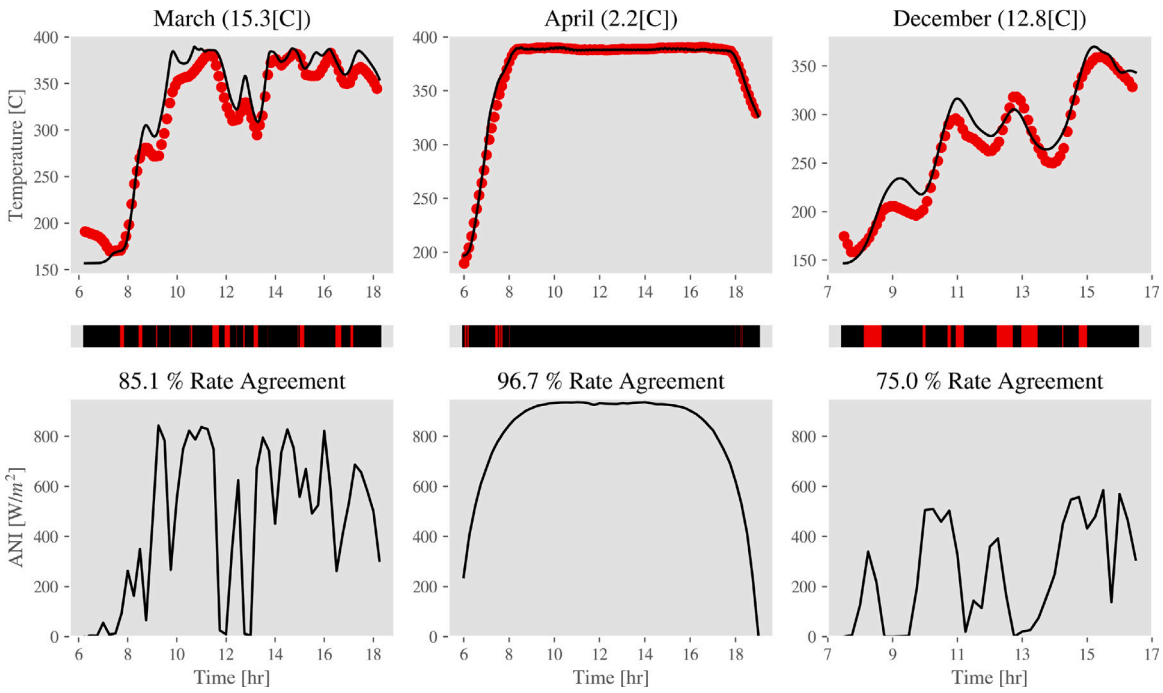

Fig. 6. Solar field sector responses for three separate days comparing simulated sector outlet temperatures (black) and measured outlet temperatures (red dots). (For interpretation of the references to color in this figure legend, the reader is referred to the web version of this article.)

3.2. Solar field sector

Fifteen-minute time-averaged operational data from Solana was used to validate the solar field sector model. The measurements include HTF flow rate through the sector, inlet HTF temperature to the sector, outlet HTF temperature of the sector, and weather/solar conditions. A solar field sector was simulated using multiple days of this data with 2-s time steps. Each solar field loop was discretized into control volumes of 4 m in length. At each time step in the simulation, the measured weather data, sector flow rate, and inlet temperature to the sector were used as inputs for the model. The model then computed the outlet temperature of the solar field sector throughout the day. Fig. 6 presents the HTF temperature at the sector outlet as computed by the model (black) and as measured during operation (red) for three separate days.

Each column of Fig. 6 corresponds to a day simulated in the specified month along with the mean absolute error over the evaluation horizon between simulated and measured sector outlet temperatures. Solar field outlet temperatures are provided in the top plot, and aperture-normal irradiance (ANI), the DNI normal to collector, is presented in the bottom plot. The black/red color bar indicator below the temperature plots displays agreement between simulated and measured temperature derivatives. Black indicates that the first derivative of temperature with respect to time of the simulation and measured data (positive, negative, or near zero) are aligned, while red denotes rate disagreement. The total rate agreement is defined as the number of black marks divided by the total number of marks. With all days exhibiting rate agreement greater than 75%, this case study suggests that the solar field sector model predicts the transient temperature response well even on challenging cloudy days where the DNI likely has spatial variability across the sector.

In addition to sector temperature data, the validation dataset also specifies the sector-averaged degrees of defocus for each SCA in a loop, including those that are not presently defocused. The defocusing control strategy employed during operation for the validation dataset differs from the strategy implemented in the model, so comparisons were made via total optical efficiency of the loop as opposed to directly comparing defocusing degree measurements. The intercept factor curve presented in Fig. 4 relates collector defocusing in degrees to a loop optical efficiency value. Loop optical efficiency is computed using Eq. (11).

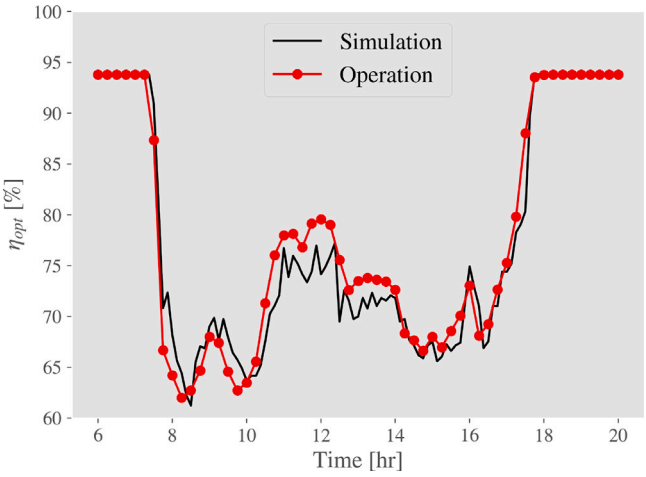

Fig. 7. Intercept metric comparing heat rejection via defocusing for the model (black) and operation (red). (For interpretation of the references to color in this figure legend, the reader is referred to the web version of this article.)

$$\eta_{opt} = \frac{1}{n_{SCA}} \sum_{i=1}^{n_{SCA}} f_{IC}(\theta_i) \tag{11}$$

In this equation, η_{opt} is total optical efficiency of the loop, θ_i is the average number of degrees the ith SCA is defocused, and $f_{IC}(\cdot)$ is the function that maps degrees defocused to the intercept factors computed using SolTrace. The optical efficiency has a minimum of 0% when all of the SCA's are defocused and has a maximum of 100% when zero SCA's are defocused and the collectors have perfect optical properties. Geometric imperfections of the collector preclude η_{opt} from achieving 100%. Fig. 7 shows the loop optical efficiency as obtained from the operational data (red) and as computed by the simulation (black) for the sunny April day presented in Fig. 6.

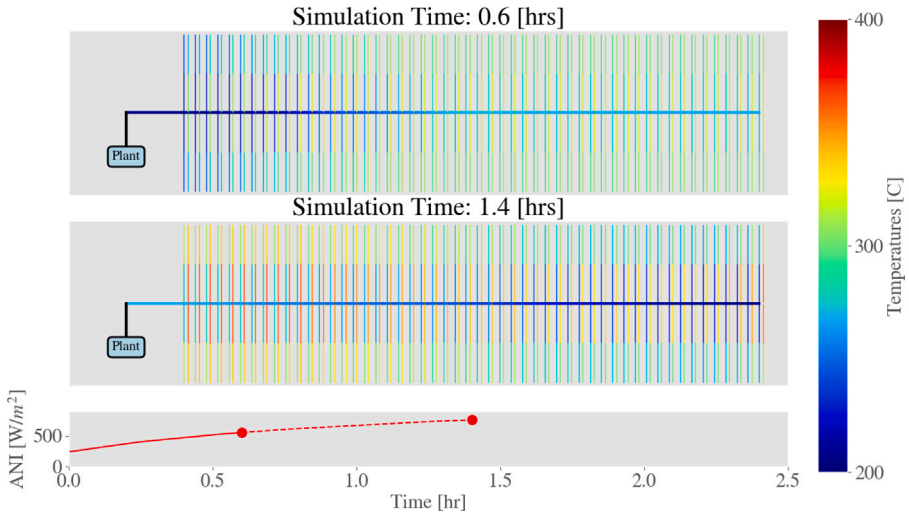

Fig. 8. Solar field sector temperature distribution during start up with cold slug moving through it.

Consistent agreement is observed between the loop optical efficiency values computed with operational defocusing and simulation defocusing for the relatively sunny day in question. Coupling this result with the accuracy of sector outlet temperature from Fig. 6 suggests that the thermal behavior of a sector is captured well by the model.

4. Case studies

This section presents case studies that illustrate the novel capabilities of this solar field model. The first study focuses on a user-controlled solar field startup. This study demonstrates the prediction of pump cavitation and the transient, coupled behaviors that operators can expect at a plant. The next study explores the model's utility in enhancing plant design and operational strategies by investigating net electricity production as a function of realistic distributions of mass flow rates through loops in a sector.

4.1. Solar field start up

A solar field representing a plant similar to Solana is implemented in TRNSYS and couples the previously-discussed hydraulic solver with the solar field sector models. The complete solar field model is comprised of eight unique solar field sectors, ten HTF pumps operating in parallel, runner pipes to supply and return HTF from the sectors, sector control valves, bypass control valves, central plant control valves, and an expansion system. The capability of the model was tested via a simplified interactive graphical user interface (GUI) that was developed to facilitate user interaction during a start-up sequence after sunrise. The simplified interface allows users to adjust pump speeds and valve positions in a manner consistent with actual plant operations.

To capture the realistic behavior operators are expected to manage, every loop in each sector is simulated with each having unique performance and temperature output. One case in which this variability is prominent occurs during most early morning start ups when a "cold slug" of HTF (i.e., a contiguous volume within a pipe or set of adjacent pipes) forms as a result heat loss from valve-isolated sections of piping during the night. This HTF is introduced to the solar field inlet header after the isolation valves are opened during the warm-up process, causing a significant drop in HTF temperature at the inlet of each loop as the fluid travels through the field. Fig. 8 shows the temperature response for each SCA and loop in the field to the cold slug for one of the eight sectors at two points in time.

These results highlight the complex dynamics within the sector that are not adequately captured by scaling the performance of a single loop or small set of representative loops, as has been done previously. Furthermore, sector temperatures are often summarized using the mean temperature at the 4th SCA across all constituent loops. However, this simplification overlooks the actual temperature distribution which should be properly understood to improve startup practices, avoid excessive defocusing, select optimal HTF flow rates, and identify under-performing units.

As previously mentioned, the model captures the complex interplay between the temperature of the HTF in the field, expansion tank level, and pump speeds to predict pump cavitation. Operators often want to increase pump speeds during startup to decrease the time it takes for HTF to return to the central plant from the solar field. However, increasing pump speeds too quickly can lead to pump cavitation without sufficient fluid level in the expansion tank and the concomitant NPSHR at the pump inlet. The present work is well-positioned to simulate this type of upset condition, as shown in Fig. 9 which illustrates a modeled start-up sequence in which an operator increases pump speeds without sufficient NPSHR and consequentially causes HTF pump cavitation.

The operating scenario in Fig. 9 is now discussed in more detail to illustrate both the system behavior and to give an example of the operational complexity faced by plant operators. Pump cavitation is indicated in Fig. 9(a) with a value of 1, while the operator-specified pump speed is shown in Fig. 9(b), and the simulated expansion tank level and near-field HTF outlet temperature are shown in Fig. 9(c) and (d), respectively. The following procedure is employed:

1. The pump speed is increased from 10% to 20% at $t = 3$ min. *Remark*: No cavitation is present.
2. The pump speed is increased to 30% at $t = 4$ min. *Remark*: Cavitation is indicated.
3. The pump speed is decreased by the operator to 20% at $t = 4$ min, 40 s. *Remark*: Cavitation resolves.
4. A period of time passes during which the HTF temperature in the solar field increases. *Remark*: Increased temperature is accompanied by HTF expansion and an increase in the level in the expansion tanks, thereby raising the net positive suction head available to the pumps.
5. The pump speed is increased to 30% at $t = 10$ min. *Remark*: Cavitation is indicated.

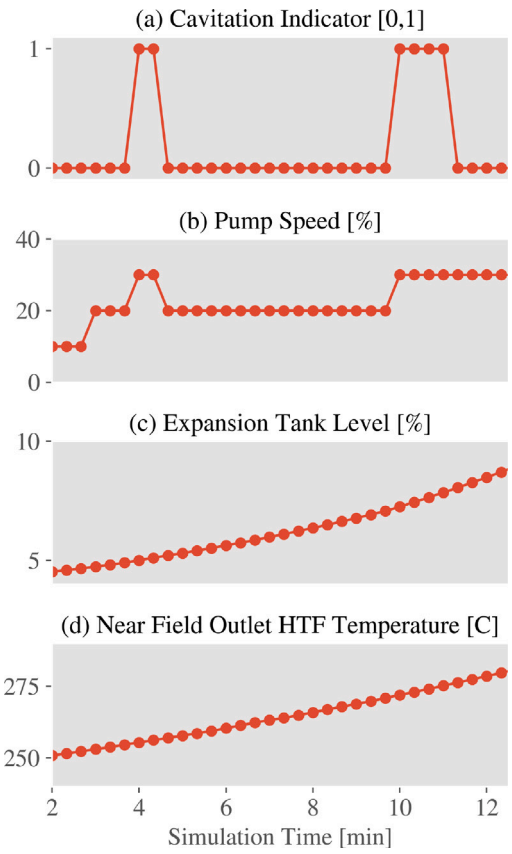

Fig. 9. User-induced pump cavitation due to insufficient level in the expansion tanks during a startup sequence.

6. No action is taken, and the pumps continue to cavitate for a period of time until the expansion tank level reaches approximately 9%. *Remark*: With sufficient NPSHR, cavitation resolves without further operator action.

This scenario illustrates an important training scenario predicted by the model that can be used to prevent damage to the pumps during actual plant operations.

As a final note, while this complete solar field model has a high level of detail and captures realistic transient effects observed at Solana, it takes around 50 ms to solve each of the 2-s time steps used in this case study (using the same computer described in Section 2.3). At a baseline of 1-s time steps, the model would therefore run 20× faster than real time.

4.2. Loop mass flow rate variability

Achieving balanced flow across loops in a sector is difficult in practice and variability persists, presenting a challenge for optimal plant control. Many plants utilize flow rate controls that adjust pump speeds to achieve a target HTF temperature set point at the loop outlet. However, defocusing occurs when individual loop HTF temperatures exceed an upper limit, which can be caused by relatively low flow compared to other loops fed by the same header system. There exists a fundamental tradeoff between energy and exergy in this situation: in one case, thermal energy collection is maximized by operating at a high flow and lower mean loop outlet HTF temperature, while in the converse case, the thermodynamic conversion efficiency in the power cycle is maximized by producing HTF at the highest possible temperature. This model is well-positioned to investigate the tradeoff between high outlet temperatures and these losses in the context of net power production as a function of variability in loop flow rates. The following analysis investigates the sector HTF flow rate that maximizes net electricity production with variability in loop flow rates.

To begin, we define an idealized baseline mass flow rate through a sector with 104 loops using weather data from a sunny April day in Gila Bend, AZ. The inlet HTF temperature to the sector is held constant, and flow is equally distributed across the loops. An HTF flow rate profile is computed for the analysis day such that all loops have an outlet temperature of 390 [°C] without requiring any defocusing. This flow rate profile serves as the baseline for subsequent analyses. Next, simulations were repeated for the same day in order to conduct a parametric sweep of relevant mass flow rate parameters. In this study, there are two parameters of interest. The first is mass flow variability among loops, σ, which was introduced in Eq. (9). Recall, the flow rate for each loop is determined based on the average flow rate through a loop multiplied by a randomly-sampled adjustment factor. At the beginning of the simulation, this adjustment factor is generated for each loop from a zero-mean normal distribution with a standard deviation of σ.

The second sweep parameter corresponds to the total amount of mass flow through the sector. Sector mass flow rates were adjusted with Eq. (12). At each timestep, t, the sector model takes in the baseline mass flow rate adjusted by the parameter Z. Thus, the baseline mass flow rate profile for the day is modified uniformly by Z.

$$\dot{m}_{sector,t} = (1 + Z)\ \dot{m}_{baseline,t} \tag{12}$$

Next, the net electricity production over the day is computed to quantify the effects of different flow rate profiles. First, Eq. (13) computes the total rate of heat absorption by the sector, $\dot{W}_{sector,t}$, which depends on the sector HTF mass flow rate, $\dot{m}_{sector,t}$, and the difference of HTF temperatures at the inlet and outlet of the sector.

$$\dot{W}_{sector,t} = c\ \dot{m}_{sector,t}\ (T_{HTF,out,t} - T_{HTF,inlet,t}) \tag{13}$$

Here, c is the specific heat of the HTF at the mean temperature within the sector. While total heat absorbed is an important measure, the ultimate goal is to maximize the net electricity. Eq. (14) calculates $\dot{W}_{e,t}$, the net electrical power output, and it accounts for the efficiency of the power cycle, $\eta_{plant,t}$, along with the power consumption of the pumps, $\dot{W}_{pump,t}$.

$$\dot{W}_{e,t} = \dot{W}_{sector,t}\ \eta_{plant,t} - \dot{W}_{pump,t} \tag{14}$$

The efficiency of the power plant, $\eta_{plant,t}$, is estimated using the Carnot efficiency modified by a factor b which reflects real-world deviations from ideal performance. While the factor b remains constant, the Carnot efficiency is subject to change based on the temperature of the HTF leaving the sector.

$$\eta_{plant,t} = \underbrace{\left(\eta_{plant,ref}\ \left(1 - \frac{T_{cold,ref}}{T_{hot,ref}}\right)^{(-1)}\right)}_{b} \left(1 - \frac{T_{cold}}{T_{hot,t}}\right) \tag{15}$$

The Carnot efficiency is a function of the hot and cold temperatures that are inputs to the power cycle. In this study, the cold temperature is assumed to be constant at 15 [°C], and the hot temperature corresponds to the temperature of the HTF at the sector outlet which is subject to change. Furthermore, the multiplier factor, b, is computed by assuming the power cycle has an efficiency of about $\eta_{plant,ref} = 35.6\%$ when $T_{hot,ref} = 391$ [°C]. For subsequent calculations, the multiplier b remains constant and can be used to estimate the efficiency of the power cycle for various sector outlet temperatures.

Additionally, the power required for the pump operation, computed with Eq. (16), is a function of the pressure drop across the sector, $\Delta P_{sector,t}$, the volumetric flow rate of HTF, $\dot{Q}_{HTF,t}$, and the

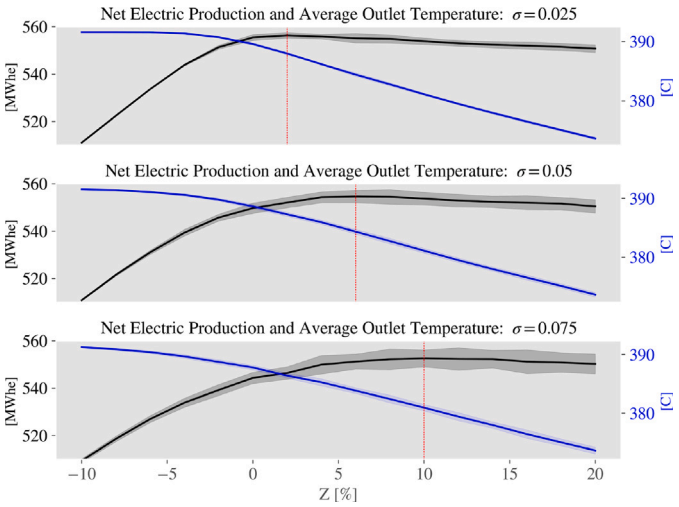

Fig. 10. Net electricity production (black) and average sector outlet temperature (blue) for σ = 0.025, 0.05, 0.075 as a function of total flow through the sector. (For interpretation of the references to color in this figure legend, the reader is referred to the web version of this article.)

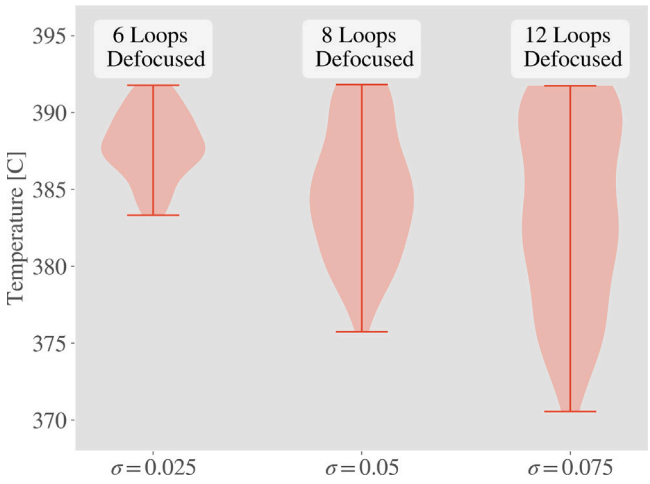

Fig. 11. Loop outlet temperature histogram for different values of mass flow variability at the selected optimal flow condition.

pump efficiency, η_{pump}. The pump efficiency, defined as the fraction of mechanical power converted from electrical power, is assumed to be constant.

$$\dot{W}_{pump,t} = \frac{\Delta P_{sector,t}\ \dot{Q}_{HTF,t}}{\eta_{pump}} \tag{16}$$

Lastly, the net power is integrated over the day to calculate the net energy produced by the solar field using Eq. (17). This metric is ultimately used to compare the performance of the sector with varying flow rates.

$$E = \int_{t_{start}}^{t_{end}} \dot{W}_{e,t}\, dt \tag{17}$$

The model was employed to determine the optimal mass flow rate profile by sweeping over a range of Z values for three different loop mass flow variability values ($\sigma = [0.025, 0.05, 0.075]$), corresponding to an expected 95% of loop mass flow rates falling within ±5%, ±10% and ±15% of the mean loop flow rate, respectively. Because mass flow variability is sampled from a normal distribution, forty replicates were performed with loop properties newly sampled for each unique combination of σ and Z. Fig. 10 presents the integrated net electricity production and average HTF sector outlet temperature as a function of the mass flow multiplier Z for each flow variability parameter σ. The envelope around each line indicates one standard deviation of the population of results at each combination of Z and σ, and the solid line represents the average value. Additionally, the red vertical line indicates the Z value at which total net electricity generation is maximized.

Several observations are noted as follows: Firstly, as the variability in mass flow rates (σ) increases, the flow rate profile (adjusted by Z) that maximizes total net electricity generation shifts higher. At the same time, the maximum net electricity that can be achieved decreases. Secondly, higher mass flow rates lead to a decrease in the average HTF sector outlet temperature as can be intuitively expected from an understanding of the solar field energy balance. Conversely, lower flow rates have the opposite effect.

The finding that the optimal Z values and σ values are positively correlated can be understood in terms of the distribution of loop outlet temperatures relative to the maximum cutoff (defocusing) temperature. Fig. 11 displays the loop outlet temperature distribution for the optimal mass flow rate associated with each σ level where the width of the plot indicates the number of loops producing HTF at the corresponding temperature.

Fig. 11 captures the balance between the opposing effects of defocusing losses and cycle conversion efficiency. For sectors with lower loop flow rate variability (σ = 0.025), the temperature distribution is tightly concentrated, allowing higher average HTF temperatures with fewer loops exceeding the temperature limit in the optimal flow case. On average, only 6 of 104 loops require defocusing for this value of σ. In contrast, the temperature distribution expands significantly with higher flow variability parameters (σ = 0.05 and σ = 0.075). Consequently, a higher number of loops must defocus even at lower average HTF temperatures. On average, 8 and 12 loops experience defocusing for σ values of 0.05 and 0.075 respectively. This study illustrates the difficult challenge plant operators experience when attempting balance defocusing losses and high HTF temperatures.

Ultimately, this study provides several insights for the operation of large CSP plants. Firstly, these systems are strongly incentivized to maintain equal flow distribution among their loops because it enhances net electricity production and allows the plant to achieve higher average HTF temperatures. However, given the prevalent variability in flow distribution across most large CSP plants, it is advantageous to adjust flow rate control to target somewhat lower sector outlet temperatures at the expense of cycle conversion efficiency. For instance, with σ = 0.05, the controller should aim for an outlet temperature of 384 [°C] to maximize net electricity production. Attempting to maintain the original set point of 390 [°C] would cause significantly more loops to defocus, leading to dumped energy that results in an approximate 20 [MWhe] decrease in electricity generation per day. The ramifications of attempting to achieve high sector outlet temperatures with larger σ values are increasingly detrimental. For example, with σ = 0.075, the decrease in electricity generation could amount to about 30 [MWhe] per day if the target remained 390 [°C]. Aside from the immediate impact on daily energy production, lowering the temperature set point could also improve the longevity of the plant. Using lower temperature set points results in fewer loops defocusing which in turn reduces the overheating of HTF. This mitigates the degradation of HTF at high temperatures that typically leads to hydrogen generation, exacerbating thermal losses to the environment and leading to a less efficient solar field over time.

5. Discussion and conclusions

This paper introduces a novel solar field model that leverages a NN to efficiently compute the heat absorbed by the HTF under various

receiver conditions. The NN approach was validated through a detailed model comparison, achieving an average difference in heat absorption of 0.3%. The solar field model's accuracy was validated against operational plant data for both temperature and defocusing efficiency.

The primary advancement of this work is the ability to model the thermal and hydraulic responses and upset conditions of a non-pristine solar field in a computationally efficient manner. The solar field model runs 20× faster than real-time at 1-s time steps and provides a foundation for a detailed operator training simulator that includes a full, coupled plant model. The simulator seeks to provide operators with a low-risk environment for skill development and experimentation with new operational strategies.

The computationally efficient model is capable of simulating realistic phenomena including loop mass flow variability and transient conditions. This work suggests guidelines for HTF setpoint temperature selection in large solar fields with loop mass flow variability. Lastly, the model seeks to replicate the actual control decisions faced by operators with respect to plant dynamics, including pump speed, cavitation, expansion system levels, and HTF temperature management.

CRediT authorship contribution statement

Matthew J. Tuman: Writing – original draft, Visualization, Validation, Software, Methodology, Investigation, Formal analysis, Data curation. **Michael J. Wagner:** Writing – review & editing, Visualization, Supervision, Resources, Funding acquisition, Conceptualization.

Declaration of Generative AI and AI-assisted technologies in the writing process

During the preparation of this work the authors used ChatGPT in order to improve writing clarity. After using this tool, the authors reviewed and edited the content as needed and take full responsibility for the content of the published article.

Funding

The work was performed with funding from the U.S. Department of Energy under grant number DE-EE0009803.

Declaration of competing interest

The authors declare that they have no known competing financial interests or personal relationships that could have appeared to influence the work reported in this paper.

Acknowledgments

The authors acknowledge Professor Douglas Reindl for his guidance and valuable feedback on the model and the paper contents. The authors furthermore acknowledge Sara Trujilo and Frederick Redell of Atlantica Sustainable Infrastructure; their critical contributions include thorough responses to our questions, facilitation of site visits, and providing Solana operational data. Lastly, we acknowledge Hank Price of Solar Dynamics, LLC, for private communications regarding CSP plant design and operations.

References

[1] M. Mehos, H. Price, R. Cable, D. Kearney, B. Kelly, G. Kolb, F. Morse, Concentrating Solar Power Best Practices Study. NREL/TP-5500-75763, Tech. Rep., National Renewable Energy Laboratory, 2020.

[2] H. Price, A parabolic trough solar power plant simulation model, in: Proc. International Solar Energy Conference, Hawaii Island, Hawaii, 2003, p. 44241.

[3] N. Blair, M. Mehos, C. Christensen, Sensitivity of concentrating solar power trough performance, cost, and financing with the solar advisor model, in: Proc. SolarPACES Symposium, Las Vegas, Nevada, 2008, 928608.

[4] M. Wagner, P. Gilman, Technical Manual for the SAM Physical Trough Model. NREL/TP-5500-51825, Tech. Rep., National Renewable Energy Laboratory, 2011.

[5] R. Forristall, Heat Transfer Analysis and Modeling of a Parabolic Trough Solar Receiver Implemented in Engineering Equation Solver, Tech. Rep., National Renewable Energy Laboratory, 2003.

[6] I.L. Garcia, J.L. Alvarez, D. Blanco, Performance model for parabolic trough solar thermal power plants with thermal storage: Comparison to operating plant data, Sol. Energy (2011).

[7] S. Quoilin, A. Desideri, J. Wronski, I. Bell, V. Lemort, ThermoCycle: A modelica library for the simulation of thermodynamic systems, in: Proc. International Modelica Conference, Lund, Sweden, 2014, pp. 683–692.

[8] J. Carballo, J. Bonilla, M. Berenguel, P. Palenzuela, Parabolic trough collector field dynamic model: Validation, energetic and exergetic analyses, Sol. Energy (2018) 777–786.

[9] R. Dickes, A. Desideri, V. Lemort, S. Quoilin, Model reduction for simulating the dynamic behavior of parabolic troughs and a thermocline energy storage in a micro-solar power unit, in: Proc. International Conference on Efficiency Cost Optimization Simulation and Environmental Impact of Energy Systems, Pau, France, 2015, pp. 1–12.

[10] Q.A. Buch, R. Dickes, A. Desideri, V. Lemort, S. Quoilin, Dynamic modeling of thermal systems using a semi-empirical approach and the ThermoCycle modelica library, in: Proc. International Conference on Efficiency Cost Optimization Simulation and Environmental Impact of Energy Systems, Pau, France, 2015, 150502.

[11] A. Desideri, R. Dickes, J. Bonilla, L. Valenzuela, S. Quoilin, V. Lemort, Steady-state and dynamic validation of a parabolic trough collector model using the ThermoCycle modelica library, Sol. Energy (2018) 866–877.

[12] K. Noureldin, Modelling and Control of Transients in Parabolic Trough Power Plants with Single-Phase Heat Transfer Fluids (Ph.D. thesis), North Rhine-Westphalia Technical University of Aachen, 2018.

[13] K. Noureldin, T. Hirsch, R. Pitz-Pall, Virtual solar field - validation of a detailed transient simulation tool for line focus STE fields with single phase heat transfer fluid, Sol. Energy (2017).

[14] D. Hoegemann, K. Noureldin, F. Bamberger, T. Hirsch, Development of training simulator software for molten salt parabolic trough test platform, in: Proc. SolarPACES Symposium, Casablanca, Morocco, 2018, 170005.

[15] T. Wendelin, A. Dobos, A. Lewandowski, SolTrace: A Ray-Tracing Code for Complex Solar Optical Systems, Tech. Rep., National Renewable Energy Laboratory, 2013.

[16] A. Elsheikh, S. Sharshir, M. Elaziz, A. Kabeel, W. Guilan, Z. Haiou, Modeling of solar energy systems using artificial neural network: A comprehensive review, Sol. Energy (2019).

[17] I. Farkas, P. Geczy-Vig, Neural network modelling of flat-plate solar collectors, Comput. Electron. Agric. (2003).

[18] J. Martinek, M.J. Wagner, Efficient prediction of concentrating solar power plant productivity using data clustering, Sol. Energy (2021).

[19] M.J. Tuman, M.J. Wagner, Informed feature selection for data clustering of CSP plant production, in: Proc. SolarPACES Symposium, Albuquerque, New Mexico, 2022, p. 651.

[20] S. Klein, et al., TRNSYS 18: A transient system simulation program, 2024, URL https://www.trnsys.com/index.html.

[21] G. Maps, Satellite imagery, 2024, URL https://www.google.com/maps. (Accessed September 2024).

[22] R. Jeppson, Steady Flow Analysis of Pipe Networks - An Instructional Manual, Utah Water Research Labratory, 1974.

[23] K. He, X. Zhang, S. Ren, J. Sun, Delving deep into rectifiers: Surpassing human-level performance on ImageNet classification, in: Proceedings of the IEEE International Conference on Computer Vision, ICCV, 2015, pp. 1026–1034.

[24] D.P. Kingma, J.L. Ba, Adam: A method for stochastic optimization, 2014, arXiv preprint arXiv:1412.6980. URL https://arxiv.org/abs/1412.6980.

[25] M.J. Tuman, Real-Time Simulation of a Parabolic Trough Solar Field Master's thesis, University of Wisconsin–Madison, 2024.

[26] F. Burkholder, C. Kutscher, Heat Loss Testing of Schott's 2008 PTR70 Parabolic Trough Receiver, NREL/TP-550-45633, Tech. Rep., National Renewable Energy Laboratory, 2009, URL https://www.osti.gov/biblio/1369635.